

Advancing Autoignition Testing Improvements in ASTM-E659 Testing Standard and Apparatus

SURF Final Report

Author: Jason Kamau
Mentors: Joseph E. Shepherd and Charline Fouchier

Explosion Dynamics Laboratory
California Institute of Technology
Pasadena, CA
August, 2025

Abstract

The autoignition temperature(AIT), defined as the minimum temperature at which a fuel ignites without an external ignition source, is a crucial parameter in assessing fire hazards across many industries. The most used methodology for determining this temperature is the ASTM-E659 standard in the United States. However, the Explosion Dynamics Laboratory, under Professor Shepherd's supervision, established that the mechanisms governing autoignition remain poorly understood, particularly in complex hydrocarbon fuels. Insights into the dispersion and ignition of such fuels under the ASTM-E659 conditions have been reached thanks to an optically accessible experimental setup. The fuel of study (hexane) was injected inside a heated test cell via a syringe pump system. Flow, concentration, and temperature data were acquired via an IR laser, photodetector, thermocouples, a high-speed camera, and LabVIEW, and analysis was done via MATLAB. The cell design was updated during the project to improve the repeatability of the tests. We evaluated injection repeatability and convection effects on concentration over a couple of tests. The calculated injected moles of fuel in the cell for all the tests were approximately 91% of the predicted moles. Stronger convection, driven by vertical temperature gradients, showed faster mixing. Finally, ignition was investigated inside the cell.

Contents

1	Introduction	1
2	Methodology	2
2.1	ASTM-E659 Experiemntal Setup	2
2.1.1	Injection	2
2.1.2	Detection	3
2.1.3	Data Acquisition	4
2.2	Results and Discussion - First 30 Tests	5
2.2.1	Injection Parameters and Testing Configurations	6
2.2.2	Repeatability of Testing Method	7
2.2.3	Effects of Thermal Gradients/Convection on Fuel Behavior	9
3	Setup Modifications	10
3.1	Sliding Door Mechanism for ASTM Setup	10
3.1.1	Motivation and Initial Direction	10
3.1.2	Concept Exploration and Design Evolution	11
3.1.3	Bill of Materials	11
3.1.4	Stand and Structural Framing	11
3.1.5	Door Construction and Materials	12
3.1.6	Pulley and Counterweight System	13
3.2	Improved Insertion System	14
3.3	Minor Modifications	15
3.3.1	Laser-Shielding Enclosures	15
3.3.2	New Flushing Setup	16
3.3.3	New Background for Background Oriented Schlieren Imaging	17
4	Final Test - Ignition	17
4.1	BOS Flow Visualization Results	18
4.2	Absorption and Temperature Plot	20
4.3	New Cell Design Evaluation	20
5	Conclusions and Future Work	21
	Acknowledgements	23
	References	24
	Appendix	25

1 Introduction

Autoignition is the phenomenon wherein a substance ignites spontaneously in the absence of an ignition source, such as a flame or spark. In these cases, the necessary energy is supplied entirely through heating the surfaces in contact with the substance [1]. The phenomenon has been studied for more than a century, originally driven by concerns in process safety, as the industrial use, storage, and transport of flammable liquids became widespread. Early researchers were primarily interested in identifying a clear ignition threshold, which ultimately led to the development of standardized criteria, such as the minimum autoignition temperature (AIT) or self-ignition temperature (SIT), for a substance in air at atmospheric pressure.

Several different experimental methods were proposed in the mid-20th century to measure spontaneous ignition through heating. A major early contribution was made by Setchkin (1954) [2], whose experiments formed the basis of what later became the ASTM-E659 standard [1]. In his method, a small amount of liquid fuel (around 0.05 to 0.5 mL) is introduced into a preheated flask of hot air, and ignition is determined through visual observation and temperature measurements. While similar in spirit to the modern ASTM-E659 procedure, Setchkin's setup differed in its use of a larger flask, a specific arrangement of heating elements, and the inclusion of a stopper. Around the same time, Zabetakis et al. proposed a variation using a smaller Erlenmeyer flask, which later influenced the now-discontinued ASTM-D2155 standard [3].

One of Setchkin's important findings was that measured AIT decreases as the combustion chamber volume increases, in some cases by as much as 50–100 °C [2]. He attributed this to the lower surface-area-to-volume ratio in larger chambers, which reduces heat loss to the surroundings. Results like these made it clear that AIT is not a purely intrinsic property of a substance, but is instead strongly dependent on the testing method and apparatus. This means that understanding the experimental setup is essential if reported AIT values are to be applied in engineering analysis or design.

Although ASTM-E659 is the recognized standard today, it still faces two key limitations. First, it is highly method-dependent - factors such as the surface material of the apparatus and the duration of the experiment strongly influence the results obtained, since they correlate with heat transfer and loss. Secondly, published AIT values rarely specify the testing procedure that was used. Safety data sheets and chemical handbooks often cite numbers from secondary databases or earlier compilations without clarifying the original source or method. Many still reference outdated standards such as ASTM-D2155 or entirely different testing approaches [1]. Because AIT is known to vary significantly with apparatus and procedure, these inconsistencies make it difficult to compare values across different fuels or even across studies of the same fuel.

One of the main challenges in this work is the limited understanding of autoignition behavior under low-temperature conditions, compounded by the fact that the ASTM-E659 apparatus is not optically accessible, making it difficult to capture key processes during ignition [4]. The objectives of this study are therefore to improve the understanding, accuracy, and repeatability of autoignition measurements, and to investigate how fuel injection parameters and thermal environments influence ignition behavior. By addressing these gaps, the study aims to contribute to the optimization of current testing methods and support the advancement of the ASTM-E659 standard.

The importance of autoignition testing extends well beyond measurement itself. It provides essential data for developing and validating ignition models, which are necessary for advancing combustion research, such as work done here by the Explosions Dynamics Laboratory (EDL) at Caltech [1, 4, 5, 6]. It underpins safety protocols in the storage, handling, and transport of fuels, where even small uncertainties in ignition thresholds can have major consequences. Regulatory bodies such as the FAA and organizations like

ASTM rely on these measurements to define standards and safety margins for industry[7]. Finally, accurate AIT data supports the design of engines, reactors, and other thermal systems by ensuring that ignition hazards are properly accounted for in both normal operation and failure scenarios.

2 Methodology

2.1 ASTM-E659 Experimental Setup

The ASTM-E659 setup used for AIT testing (see Figure 1) is constructed by Professor Shepherd and Dr. Fouchier. The experimental apparatus is assembled on a 4 ft \times 3 ft Thorlabs breadboard and combines both pre-made and custom-built components, organized into three systems: injection, detection, and data acquisition.

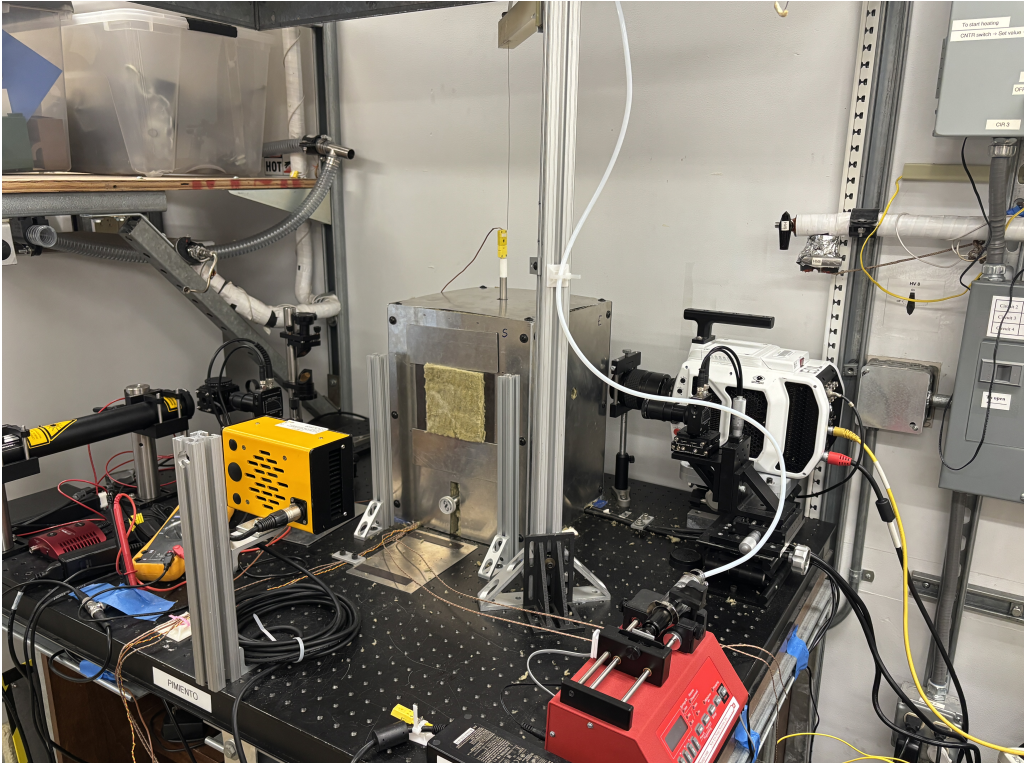
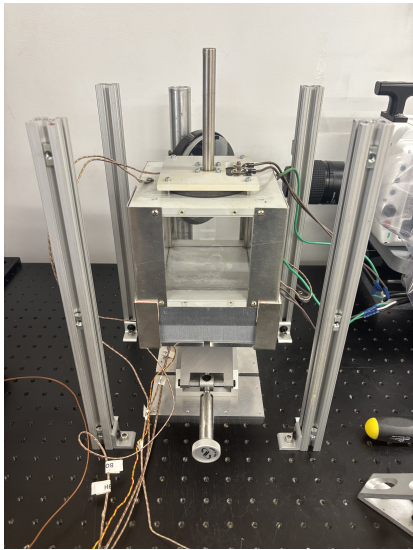


Figure 1: Photograph of the ASTM-E659 experimental setup for AIT testing, mounted on the breadboard. The system integrates injection, detection, and data acquisition subsystems using a combination of custom-built and commercial components.

2.1.1 Injection

A glass wall test cell equipped with heaters at the top of the cell provides a well-regulated environment for both fuel heating and ignition at the center of the breadboard area. This cell is surrounded by walls made of mineral wool and held in place by aluminum sheets for insulation(see Figure 2). An NE-1000 Single Channel programmable syringe pump delivers precisely metered quantities of liquid hexane, typically (for most of our experiments) 100 μL at a flow rate of 5 ml/min through a fine needle into the middle of the preheated flask (Figure 3). Hexane is selected as the test fuel because it serves as an effective surrogate for industrial fuels, such as those used in aviation. Upon injection, the hexane rapidly vaporizes and disperses throughout the chamber, mixing with the resident air to form a combustible mixture.



(a) Glass-walled test cell equipped with heaters mounted at the top to regulate fuel heating and ignition within the controlled chamber environment.



(b) Insulation system surrounding the test cell, consisting of mineral wool panels held by aluminum sheets to minimize heat loss and maintain stable operating conditions.

Figure 2: The Cell Setup



Figure 3: Syringe pump with connected pipe and injection needle used to deliver precise volumes of hexane into the test cell.

2.1.2 Detection

The detection system mainly comprises a 2mW 3390-nm infrared laser and photodetectors used to monitor the fuel concentration inside the cell during the experiment (see Figure 4). The laser beam is aligned through holes in the middle of the cell, exploiting the strong absorption of C–H bonds at this wavelength to detect the presence of hexane vapor. This system is governed by the Beer–Lambert law, which relates the transmitted laser intensity to the incident intensity through the exponential attenuation equation:

$$I = I_0 \exp(-n\sigma L)$$

I = Detected light intensity

I_0 = Incident light intensity

σ = Absorption coefficient (hexane = 40 m²/mol)

n = Concentration of hexane (mol/m³)

L = Path length the light travels through the medium (m)

As the laser beam passes through the reaction zone, absorbing molecules decrease the transmitted intensity in proportion to their concentration and the optical path length. By measuring I with respect to a known I_0 , the system quantifies absorption and thus determines real-time species concentrations during ignition. As vapor concentration increases, the transmitted laser intensity gets attenuated, and these changes are captured by photodetectors and digitized via a Picoscope for precise temporal resolution.



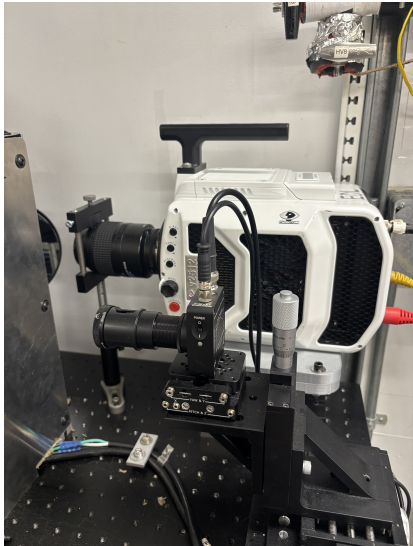
Figure 4: Detection system consisting of a 2 mW, 3390 nm infrared laser and photodetectors for monitoring fuel vapor concentration inside the test cell.

2.1.3 Data Acquisition

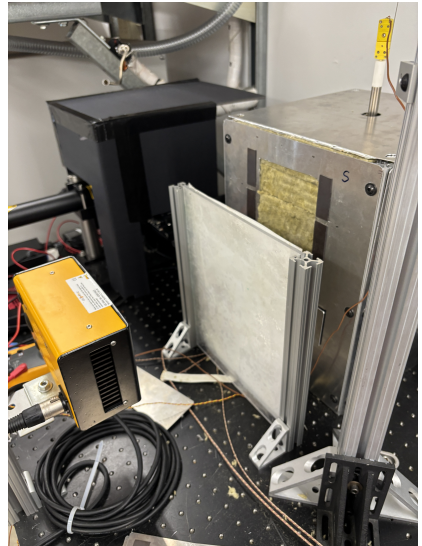
Data acquisition is done via an array of thermocouples for temperature measurements and a high-speed Phantom camera, plus a patterned background for flow-field visualization, used to complement the concentration and temperature measurements. Two thermocouples are attached to the top and bottom surfaces of the cell to monitor the temperatures of the heated surfaces, while a third thermocouple is inserted from the top into the center of the cell to measure the internal cell temperature, particularly during ignition events, for determining the autoignition temperature.

A Phantom high-speed camera is positioned in the back of the cell to enable optical visualization of the inside of the cell during the experiment. Due to limited space, the image is captured via a mirror. For flow-field visualization of the events inside the cell, a

technique known as Background-Oriented Schlieren (BOS) imaging is employed, whereby a high-contrast patterned background is placed at the front of the chamber and illuminated by a high-intensity light source (see Figure 5). For this setup, a speckled background is positioned in front of the LEDs, 2 inches from the cell. An array of LED lights is placed behind the background for illumination. The Phantom camera records refractive distortions in the background caused by density gradients, enabling visualization of vapor dispersion, mixing, and thermal convection during injection, vaporization, and ignition. The camera is controlled using PCC software, allowing selection of frame rate and exposure time. Timing and coordination of the process are governed by LabVIEW, which automates the injection and synchronizes it with all the systems above. All experimental signals - laser attenuation, high-speed imaging and recording, temperature, and timing - are logged and post-processed in MATLAB. This synchronized dataset provides a comprehensive picture of each experiment, capturing both physical and optical signatures of the process. The setup is sufficiently sensitive to resolve subtle differences arising from injection volume, thermal gradients, and convection within the flask, allowing for detailed interrogation of vaporization and ignition phenomena under controlled conditions.



(a) High Speed Camera and Mirror Setup



(b) BOS Background setup in front of the cell

Figure 5: Optical visualization system consisting of a Phantom high-speed camera positioned behind the test cell. Due to space constraints, images are captured via a mirror. Flow-field visualization is achieved using Background-Oriented Schlieren (BOS) imaging, with a high-contrast patterned background illuminated by a high-intensity light source.

Between tests, the cell is purged using a heat gun. The heated air pushes the combustion gases outside of the cell.

2.2 Results and Discussion - First 30 Tests

Over the course of 30 tests, I focused on two main objectives: evaluating the repeatability of the injection system and examining the role of convection on the behavior of the fuel inside the preheated cell. Across repeated trials, this injection protocol allows me to isolate variations in concentration from inconsistencies in fuel delivery. At the same time, by introducing controlled convection through altering the temperatures of the top and the bottom of the cell, I could observe how mixing and thermal gradients influence vaporization. Together, these two threads - system repeatability and convective effects -

frame the results that follow and provide a basis for interpreting the behavior of hexane under the test conditions.

2.2.1 Injection Parameters and Testing Configurations

The syringe injector delivers liquid hexane with a target volume of $100 \mu\text{L}$ per test, corresponding to approximately $7.66 \cdot 10^{-4}$ mol of fuel. The injection rate is maintained at 5 ml/min , ensuring a consistent and controlled delivery to the chamber. Precise volume control is essential, as even minor deviations influence the vapor concentration since the volumetric values are in the microliter range for this experiment.

Laser transmission through the test section is recorded with a Picoscope at 100 kHz and controlled with LabVIEW with an acquisition time of 5 seconds. Each run consists of two distinct measurements:

- The dark signal, collected with the shutter closed, provides the electronic baseline of the detector in the absence of light.
- The reference signal (I_0), recorded with the shutter open and before fuel injection, represents the full transmitted laser intensity through the empty chamber.

During injection, the transmitted laser intensity (I) is measured at an acquisition time of 200 s . The presence of vaporized hexane reduces the transmitted intensity through absorption and scattering, and the ratio $\frac{I}{I_0}$ is later used to quantify the vapor concentration in the chamber.

Using Beer-Lambert's equation and proper calibrations done by Professor Shepherd's team, we can acquire the concentration of hexane n (mol/m^3) from the intensity ratio and use the equations of the mole, mass, and density relation to calculate the moles of hexane over the duration of the experiment and plot these values as shown in Figure 6. Same relations can be used to acquire the final volumes of the vapor hexane inside the cell.

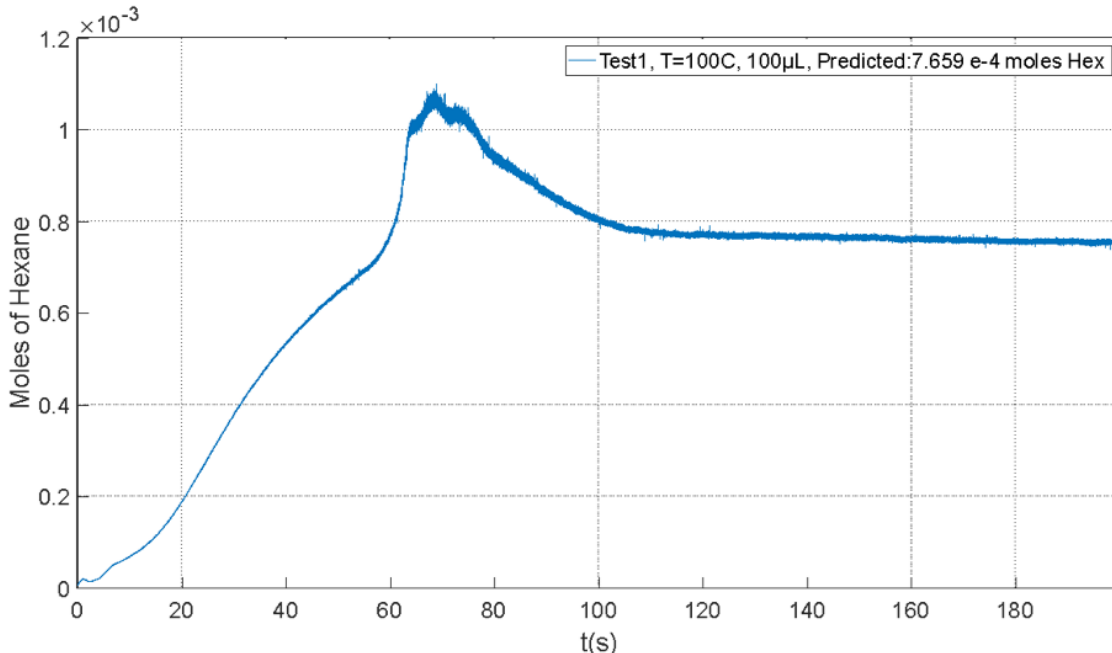


Figure 6: A plot showing the calculated hexane concentration over time.

At this stage, all experiments are conducted under nonreactive conditions, with focus solely on fuel vaporization behavior. By isolating vaporization, we can assess the repeatability of the injection system and the influence of convection on vapor distribution without the additional complexities of ignition.

2.2.2 Repeatability of Testing Method

To ensure repeatability, the experimental procedures and initial conditions are maintained under closely controlled conditions (see Appendix A). For each test, the resulting concentration-time curves were overlaid and compared against the ideal injection value ($\approx 7.66 \cdot 10^{-4}$ mol of hexane vapor). This approach provided a visual and quantitative basis for evaluating how closely individual runs aligned with the target behavior.

Various tests are represented in Figure 7. Several tests exhibited strong consistency. For instance, Test 1 and Test 8 produced nearly identical curves, with Test 8 tracking the ideal profile most closely. Similarly, Test 7 and Test 9 shared similar trends, while Test 3 and Test 10 also formed a matched pair.

During testing, certain issues were identified that occasionally disrupted injection accuracy. During Tests 7, 8, and 9, the syringe needle intermittently got stuck, producing inconsistent delivery. These issues originated with Test 5 - the first instance of needle sticking - and persisted until the setup was corrected in Tests 10–12. The repeatability window was defined by the extreme cases: the lowest curve (Test 4) and the highest curve (Test 1) from the filtered data. Most tests fell within this range, though deviations were tied to identifiable experimental issues, hence creating a repeatability window or margin for tests that would provide good data for analysis. For example:

- Test 4: slight under-injection due to a missing droplet.
- Test 5: first occurrence of needle sticking (mechanical problems)
- Test 6: formation of a hexane bubble, producing a multiphase disperse flow. This caused reduced injected volume and uneven dispersion in the flask.
- Test 11: additional fuel was unintentionally added after the first injection, artificially increasing the volume.

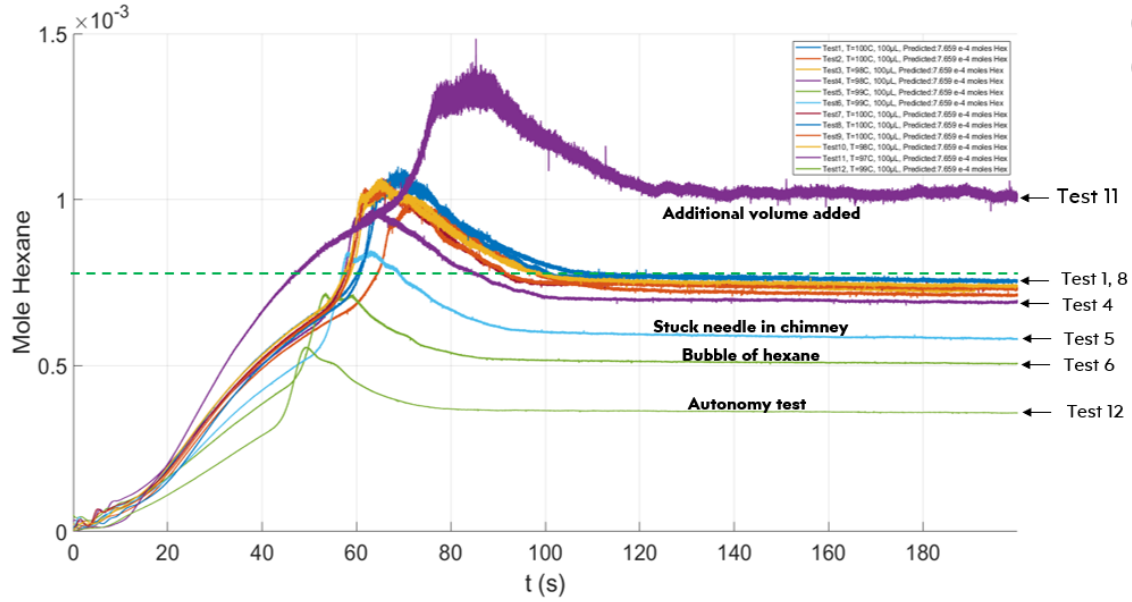


Figure 7: Overlay of concentration–time curves showing the repeatability window for hexane injections. Tests 1 and 8 align most closely with the ideal profile ($7.66 \cdot 10^{-4}$ mol) highlighted with a dotted green line, while deviations (e.g., needle sticking in Tests 5–9, bubble formation in Test 6, and extra fuel in Test 11) highlight mechanical and procedural factors affecting consistency.

After additional trials, only Test 14 matched the high-quality behavior of Tests 1 and 8, ranking as the second highest curve. Other tests coming close were 15, 16, 23, 24, 25, 27, 29, and 30 - the closest ones being 25 and 29. Other tests fell outside the repeatability window and were excluded as outliers. Data from the plotted mole concentrations at the end of the test and deviations compared to the volume injected can be seen in Figure 8 and Figure 9.

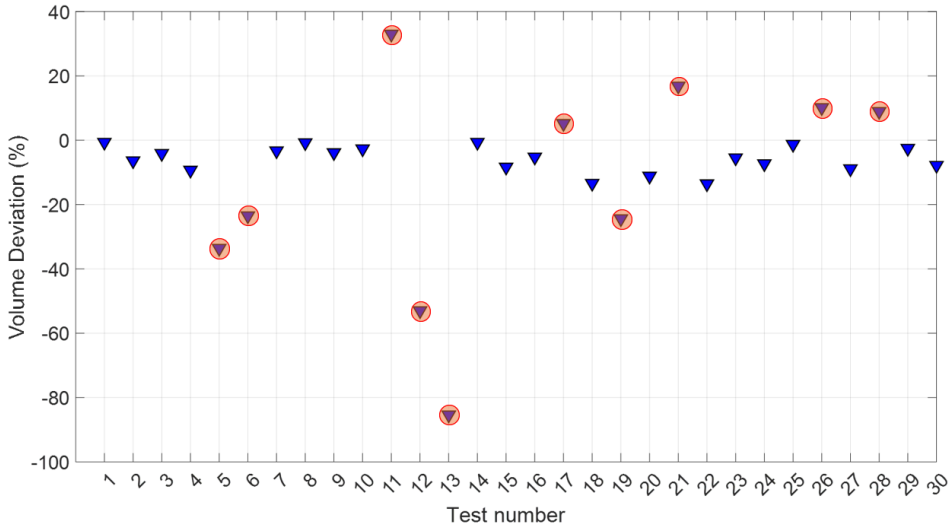


Figure 8: Volume deviation plot showing repeatability across trials. Tests 1, 8, and 14 matched best, with 25 and 29 close. Others outside the repeatability window were marked as outliers.

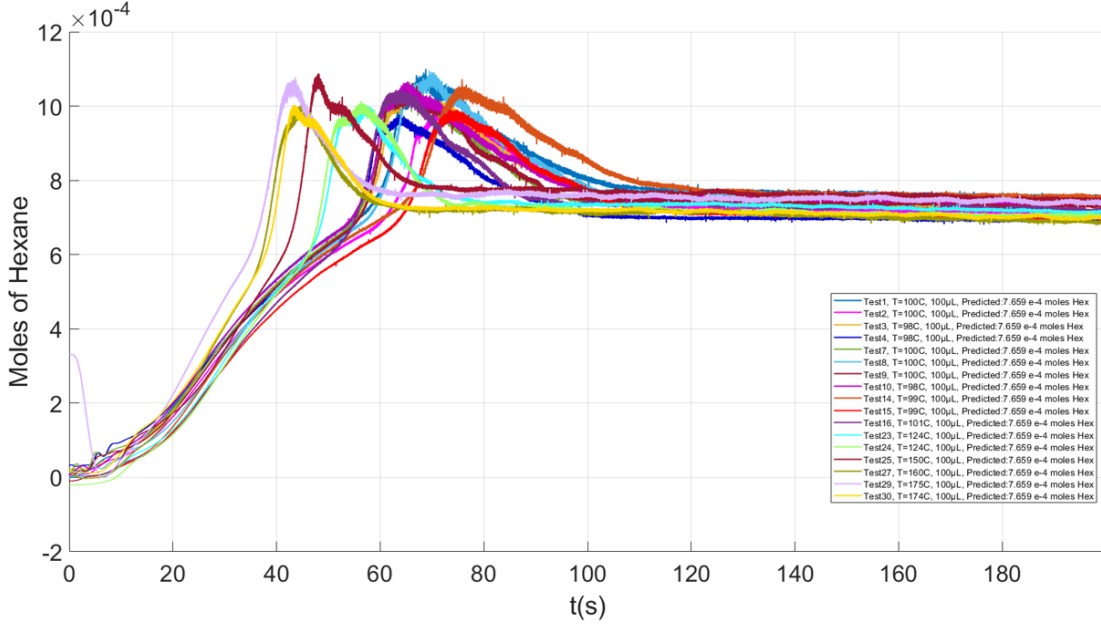


Figure 9: Overlay of concentration–time curves showing the tests that lie within the repeatability window

Using $90 \mu\text{L}$ (test 4) as a lower limit for the repeatability window, 57% of the injections fell within the acceptable range. Tightening the cutoff to $93 \mu\text{L}$ (test 3), approximately 53% of the runs still met the criterion. These results suggest that although the syringe system performs consistently on average, variability in individual tests remains a limiting factor for repeatability. Reducing this spread will be critical to drawing sharper correlations between injection parameters and ignition results in the future.

Overall, these observations highlight the sensitivity of the injection process to small procedural or mechanical deviations, particularly given the microliter-scale volumes. When equipment functioned smoothly, repeatability was strong, but mechanical faults (needle sticking, dripping, or bubbles) introduced substantial variation.

2.2.3 Effects of Thermal Gradients/Convection on Fuel Behavior

Convection effects were also apparent across the test series (see Appendix A for test gradients). Tests are given in Figure 10. Tests 7, 8, and 9 were conducted under conditions with a $4\text{--}5^\circ\text{C}$ vertical temperature gradient across the cell, yet the calculated injected volumes remained similar to those without a gradient. For small thermal gradients, convection effects appeared to have a limited influence on the measured injection volume. This also suggests that convection alters mixing dynamics but not the ultimate volume of fuel vaporized. Test 16, conducted with an 8°C thermal gradient and cell temperature of 101°C , produced a notably distinct curve, suggesting that larger gradients begin to impact the vaporization dynamics. Tests carried out at higher cell temperatures, particularly test 28 at 170°C with a vertical temperature gradient of 25°C , exhibited stronger natural convection. This enhanced mixing accelerated the transport of fuel vapor into the hot zone, which was observed as an earlier and sharper drop in laser transmission on the photodiode signal. Importantly, convection did not alter the final vapor concentration inside the flask - as predicted by the ideal gas law - but it strongly influenced how quickly that concentration was reached. This observation reinforces that mixing dynamics, not just the thermodynamic state, might play a key role in shaping ignition behavior.

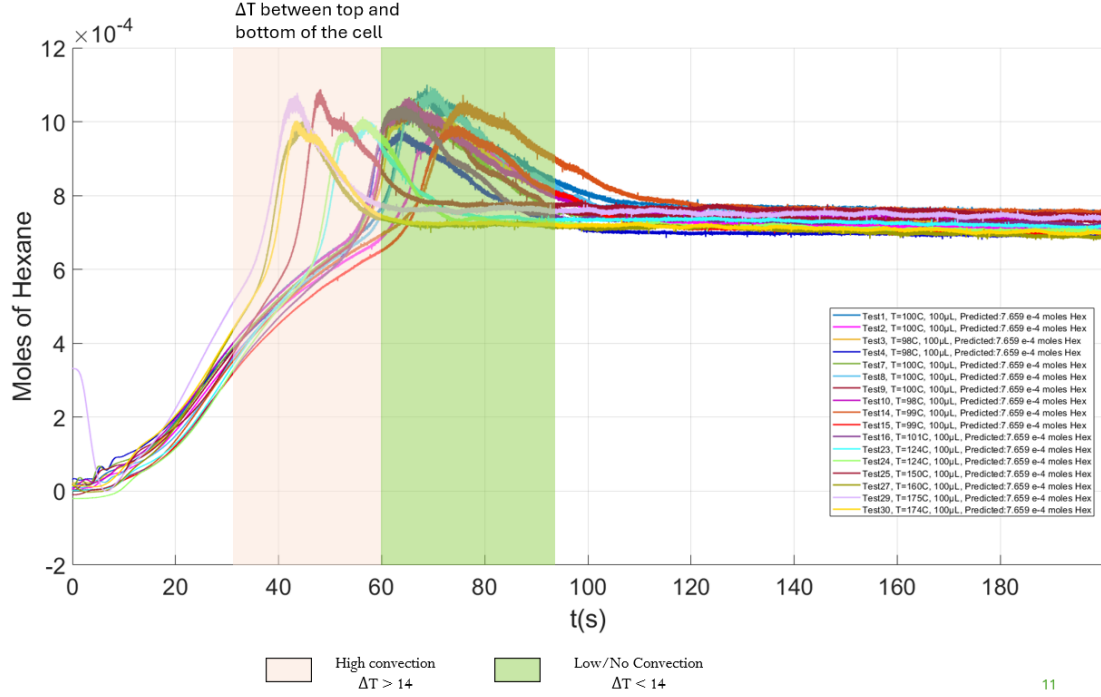


Figure 10: Effect of natural convection at higher cell temperatures, showing accelerated vapor transport and earlier laser transmission drop without altering the final vapor concentration.

The data further demonstrate the sensitivity of the ASTM-inspired setup to seemingly minor factors. Variations in pre- and post-injection procedures, small differences in heating, or even slight changes in setup alignment produced noticeable effects on the final concentration of the fuel calculated. In summary, the injector system shows solid average performance, but requires refinement to reduce variability between runs. Convection is confirmed to be a secondary but important effect, shaping the rate at which the vapor-air mixture gets fully mixed. Going forward, improving injection precision and the setup in general became essential for generating more reproducible and interpretable ignition data.

3 Setup Modifications

3.1 Sliding Door Mechanism for ASTM Setup

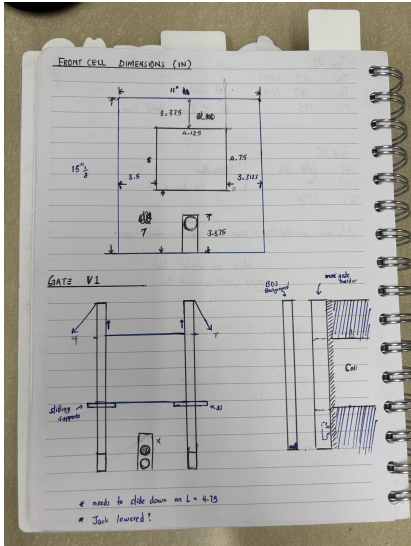
3.1.1 Motivation and Initial Direction

Our experimental setup requires placing a background-oriented schlieren (BOS) background panel, a black box for the illuminator, and two mineral wool blocks in the front and back entrances of the cell setup as shown in (Figure 3). In the previous configuration, accessing the inside of the enclosure involved fully removing the front and rear doors, followed by positioning the BOS background panel, the black box, and reattaching the insulation panels after each run. This process was time-consuming and led to slower turnaround between experiments and repeated disturbances to the thermal environment, causing heat loss and possibly variability between tests.

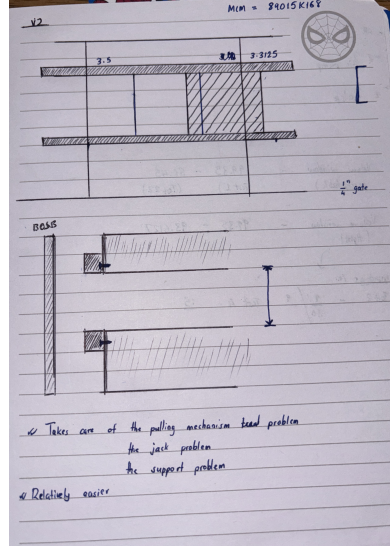
To streamline this process, I proposed and initiated a project to design a sliding door system that would allow both doors to open and close quickly, without disassembly. The system needed to be compact enough to fit inside the fume hood, structurally stable, and thermally insulated.

3.1.2 Concept Exploration and Design Evolution

The first concept was a vertically sliding door suspended by ropes connected to each side (see Figure 11). However, this approach would lead to uneven tension and unbalanced door motion, which made it unreliable. A second idea was to use a horizontal sliding door mounted on two rails. While this was mechanically straightforward, there was no simple way to ensure both doors would open and close at the same time, which was a key design requirement for sealing and convenience (see Figure 11).



(a) Initial Vertical Design



(b) Initial Horizontal Design

Figure 11: Initial door concepts: (left) vertical sliding door with rope suspension, prone to uneven tension; (right) horizontal sliding doors on rails, mechanically simple but difficult to synchronize due to spatial constraints

After several rounds of discussion and consultation, I decided on a final design: a vertically actuated, pulley-driven sliding door system. In this configuration, two doors are mounted to a rail-supported frame and lifted using a counterweight mechanism routed through a set of pulleys. This design ensures smooth and balanced motion, while keeping the structure narrow and tall to fit within the fume hood.

3.1.3 Bill of Materials

The full Bill of Materials (BOM) for the sliding door system was finalized after completion of the CAD models and approval from Dr. Fouchier and Prof. Shepherd. The parts were selected to meet mechanical, thermal, and spatial requirements of the ASTM setup and the fume hood enclosure. The table below includes all structural and mechanical components sourced or fabricated for the build. (See Appendix C)

3.1.4 Stand and Structural Framing

The frame is constructed from 5 1.5" × 1.5" single 4-slot T-slotted aluminum rails, standing 33" tall when set up. The T-slot framing serves as the main structural support for the doors and pulleys. The frame is reinforced with:

- Eight 3" silver gusset brackets at the base for lateral rigidity
- Two 90° angle brackets to secure the two vertical framing members

- Two T-brackets for mid-section connection
- Eight corner brackets for full frame integrity

All components were selected based on space constraints within the fume hood, with a vertical clearance limit of 34 $\frac{3}{4}$ " between the hood ceiling and the optical breadboard surface. The bottom two T-slotted rails were cut to 18", and the middle crossbar above them was cut to 12" to fit within the allowed dimensions. The assembled stand was mounted on a separate breadboard. Before final anchoring, all dimensions were confirmed and alignments were made to ensure no collisions with existing optical elements. The setup is shown in Figure 12.

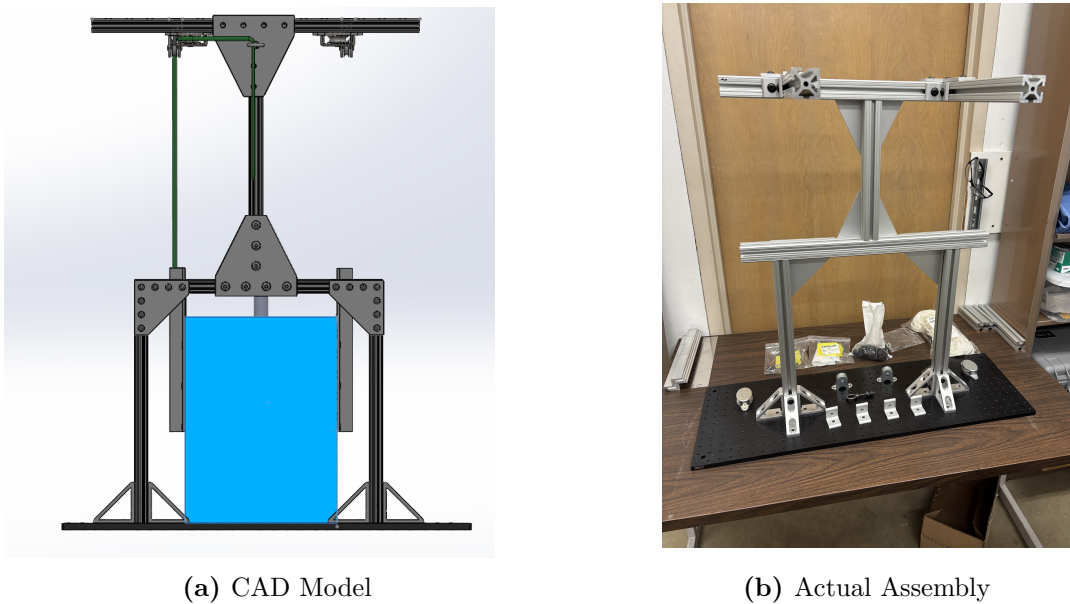


Figure 12: T-slot aluminum frame assembly (33" tall), reinforced for rigidity.

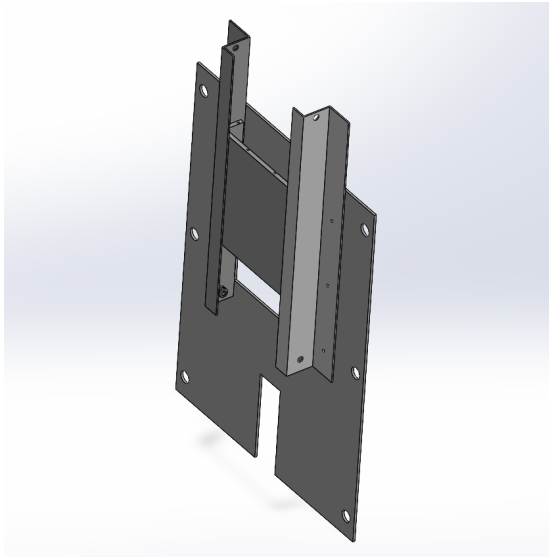
3.1.5 Door Construction and Materials

Each door is supported on both the front and back by Z-bar brackets, made from 1-1/4" \times 1-1/4", 1/16" wall-thickness aluminum stock, cut to 6" in length., which act as the guiding channels for the doors These Z-bars are attached to front and rear plates machined from 0.1" thick, 12" \times 48" aluminum sheet, using a Flow waterjet. I created the drawings in SolidWorks and exported them as DXF files for cutting.

Each Z-bar bracket is drilled with three 1/8-inch holes, spaced 3 inches apart, to accommodate screws that fasten the bars to the plates using nuts. The precision of these holes was important to ensure solid mechanical coupling and proper force distribution across the door structure.

The doors themselves were fabricated from U-channel aluminum stock, with a 3/16" wall thickness, 1" height, and 5" width, cut into 5" long sections. These U-channels form the main bodies of the sliding doors.

To enclose the U-channel and create a sealed frame for the fiberglass wool, a 0.05" thick aluminum sheet into 1" \times 5" plates was machined for both the top and bottom of each U-channel section. These plates were secured by six 2-56 screws top and bottom onto the channel in 0.07" clearance holes which were tapped, evenly spaced along the edges to hold the plates flush and rigid. The setup is shown in Figure 13.



(a) CAD Model



(b) Actual Assembly

Figure 13: Assembled stand with sliding door system laid down and disassembled doors showing Z-bar guides and U-channels.

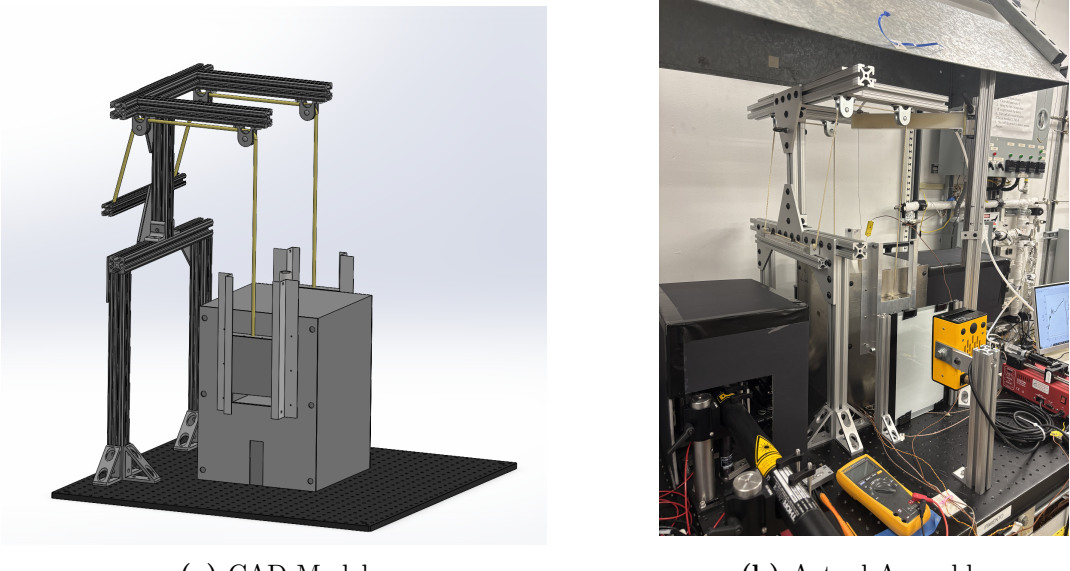
3.1.6 Pulley and Counterweight System

To control the opening and closing of the doors, I designed a pulley system mounted to the top rail. The system includes:

- Two pulleys mounted above each door
- Two redirection pulleys to guide the ropes toward the center of the frame
- Low-stretch, grip-tight rope, chosen to avoid elastic deformation during motion
- An eyebolt anchored to the central vertical rail where the ropes will go through and link where a counterweight will be attached.

Initial mechanical tests revealed several issues: horizontal pulleys and an eyebolt introduced excess friction, making vertical motion difficult; polyester rope was too flimsy and stretched under load; and the counterweight system was unstable, with the potential to fall onto sensitive laser equipment. In addition, metal-on-metal sliding between the channels and shutters created further friction and prevented smooth operation. To address these challenges, the setup was redesigned with all-vertical pulleys, a bar was used as a stable counterweight, adhesive-backed Teflon strips were applied to the channel contact surfaces to reduce friction, and the rope was replaced with a stronger braided hollow-core line.

The pulleys ensure both doors lift evenly, and a counterweight will add a restoring force that allows the user to open the doors with minimal effort while ensuring they close securely on their own. Custom T-slot nuts were fabricated, drilled, and tapped for 10-24 screws from the steel bar for pulley mounting since appropriate slot nut sizes for the setup could not be found or sold by manufacturers. The setup is shown in Figure 14b.



(a) CAD Model

(b) Actual Assembly

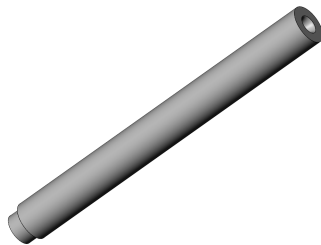
Figure 14: Final assembly of the dual-door system with vertical pulleys, counterweight bar, Teflon-lined channels, and braided rope, redesigned for smoother, safer, and more reliable operation

3.2 Improved Insertion System

During the injection phase, one recurring problem was the tendency of the syringe needle to catch on the edges of the chimney step within the cell, hence getting stuck in the process. This led to incomplete or interrupted injections, partial volume loss, and a corresponding variability in the vapor concentration achieved during tests like Test 5. Since the injected hexane volume is on the order of microliters, even small disruptions at this stage introduced significant uncertainty into the concentration field and thereby influenced the reproducibility of subsequent measurements.

To mitigate this, a guiding component was fabricated from MACOR, a machinable glass-ceramic chosen for its thermal stability and low thermal conductivity. The guide was designed with a funneled geometry: a wide inlet at the top to capture the needle reliably, tapering to a bore that closely matched the needle diameter near the bottom. This geometry ensured smooth insertion into the injection channel and eliminated misalignment at the chimney interface, thereby restoring consistency in the delivered volume (See Appendix B).

In parallel, a new 1/16" port was drilled into the cell top to accommodate the thermocouple, which had previously been housed in close proximity to the injection path. By relocating the thermocouple into a dedicated port, thermal measurements could be obtained without interfering with needle motion. This separation of functions - thermometry and fuel injection - not only reduced mechanical interference but also improved the accuracy of both measurements by decoupling them physically. The final pieces are given in Figure 15 and Figure 16.



(a) CAD Model



(b) Actual part (machined)

Figure 15: MACOR needle guide

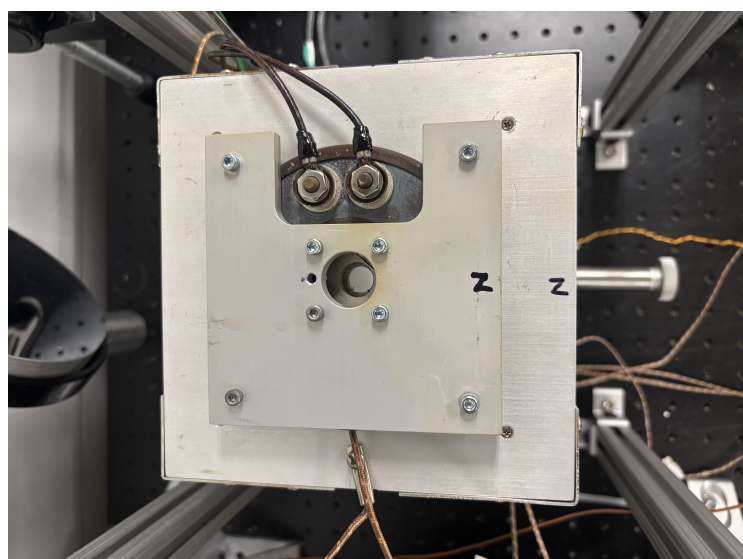


Figure 16: Relocated thermocouple port and hole leading into the cell with the step where the ceramic guide rests on.

3.3 Minor Modifications

3.3.1 Laser-Shielding Enclosures

Black foam boxes were fabricated to act as beam shields, effectively blocking stray laser light and preventing unwanted exposure to both equipment and personnel (see Figure 17).

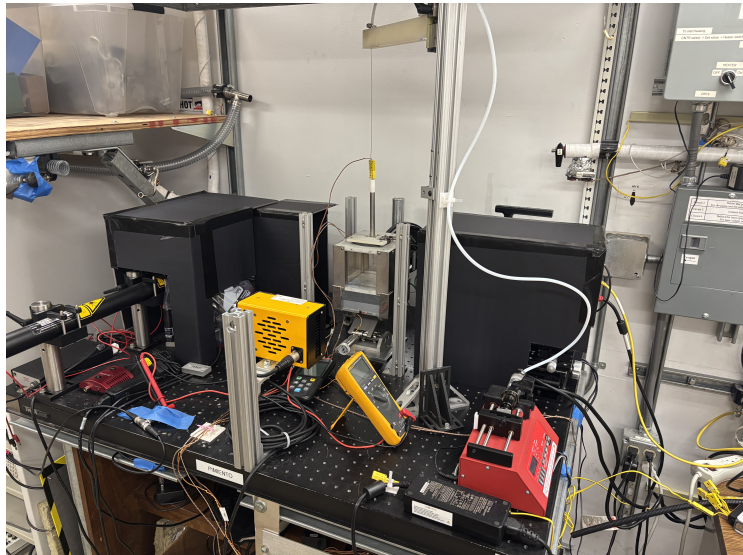


Figure 17: Black foam shielding boxes installed around beam path to block stray laser light and protect both equipment and personnel

3.3.2 New Flushing Setup

Repeated use of heat guns resulted in burnout of the heating elements after approximately five tests or more. The failure was traced to excessive pressure losses in the system, particularly due to the metal piping used to direct hot air into the cell. The mismatch in cross-sectional areas between the gun outlet and the duct amplified the pressure drop, leading to inefficient delivery of heated air and accelerated wear on the heating elements of the guns.

To address this limitation, the heat gun was replaced with a rechargeable, cordless air pump equipped with a detachable hose (see Figure 18). The device was operated at 50.0 psi, providing stable airflow without the thermal stresses associated with resistive heating. This approach eliminated the recurring burnout issue and allowed for more controlled and safer flushing of the cell environment.



(a) Metal piping used to channel hot air into the cell, which created high pressure losses and contributed to heat gun burnout.



(b) Replacement rechargeable cordless air pump and detachable hose, providing stable airflow and eliminating thermal stress issues

Figure 18: New Flushing System

3.3.3 New Background for Background Oriented Schlieren Imaging

Background Oriented Schlieren (BOS) is a flow visualization technique that measures refractive index gradients in a transparent medium. It operates by tracking displacements of a high-contrast background image, such as a speckled background, which are caused by changes in the index of refraction due to composition and density gradients. In combustion studies, this enables the visualization of fuel vapor dispersion and flame propagation, since both processes produce strong refractive index variations.

In the initial setup, the patterned background exhibited several shortcomings. The background began peeling since it was a paper background attached to glass using epoxy.

To resolve these challenges, a new high-contrast background was fabricated. The updated BOS background combines three layers, each serving a distinct function. The dotted paper provides a high-contrast reference pattern necessary for tracking image displacements. A layer of plain glass is used as a transparent support, holding the paper in place while maintaining an unobstructed view of optical distortions; this also eliminates the need for epoxy adhesives. Finally, a layer of ground glass is added to diffuse the illumination, which enhances the visibility of vapor-air mixing and liquid-gas interactions by amplifying refractive index effects. This adjustment produced sharper gradients and more stable reference images. Final setup is given in Figure 19.

Processed BOS images highlighting the vaporization process for fuels. In these images, color is scaled to the magnitude of displacement gradients: dark blue corresponds to low gradients (little to no fuel vapor present), while yellow corresponds to high gradients (high vapor concentration or the presence of liquid phase).



(a) Original BOS background with paper attached to glass using epoxy, which led to peeling after exposure to higher temperatures.



(b) New BOS background with dotted paper, plain glass, and ground glass secured by strong tape, providing higher contrast and more stable reference images.

Figure 19: New Flushing System

4 Final Test - Ignition

In this experiment, 200 μL of hexane was injected into the cell at $T(\text{cell}) = 250^\circ\text{C}$. The test successfully resulted in an ignition event, evidenced by a rapid, energetic flame that expanded quickly inside the cell. Across the broader study, ignition events were classified

into four categories along with non-ignition cases [5]:

1. Mode I (Ignition): Fast, luminous flame with rapid expansion beyond the chamber.
2. Mode II (Cool Flame): Constrained, weaker flame confined within the cell.
3. Mode III (Non-Luminous Cool Flame): Faint glow or puff of smoke with modest temperature rise.
4. Mode IV (Rapid Reaction): Short-lived, non-luminous event with small, fast temperature increase.

The test characteristics clearly matched Mode I, consistent with low ignition temperature and high vapor reactivity.

4.1 BOS Flow Visualization Results

The Background Oriented Schlieren (BOS) technique was applied by Dr. Fouchier to visualize vapor dispersion prior to ignition. Results during injection, dispersion and ignition are given in Figures 20 to 24.

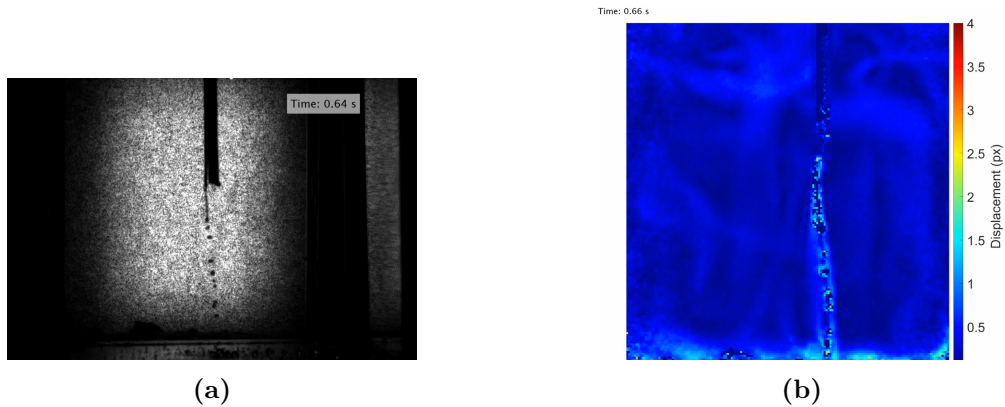


Figure 20: Fuel Injection into the preheated cell. Hexane is seen vaporizing and begins to spread radially outward.

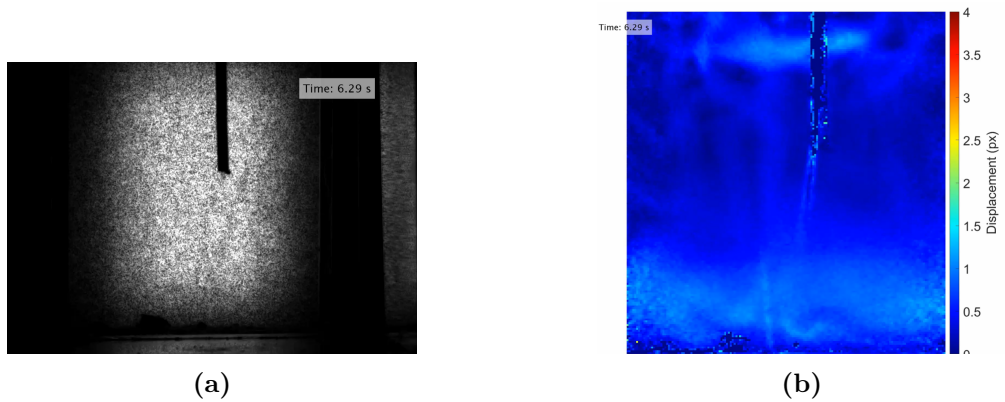


Figure 21: Immediately after injection, with vapor beginning to accumulate, intermediate mixing can be observed where diffusion and weak convection broaden the vapor cloud.

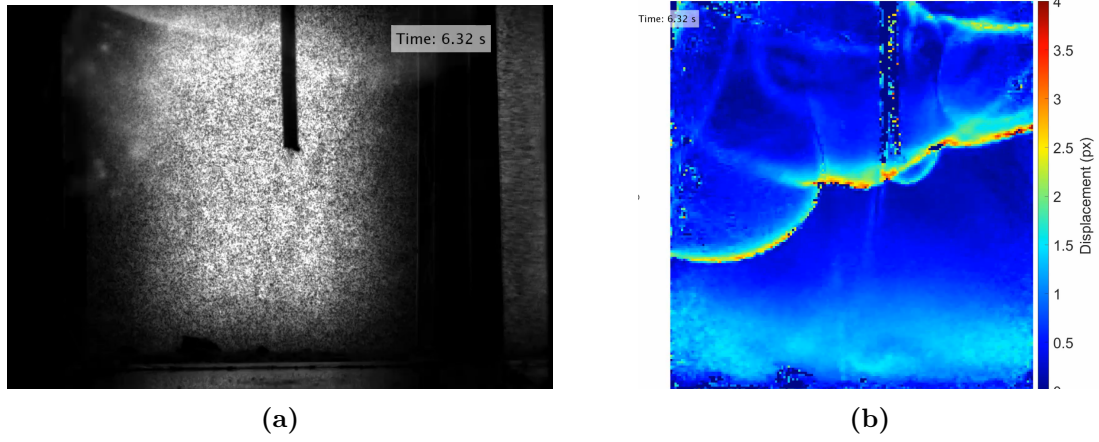


Figure 22: At around 6.32s, ignition occurs, and a sharp refractive boundary sweeps through the field

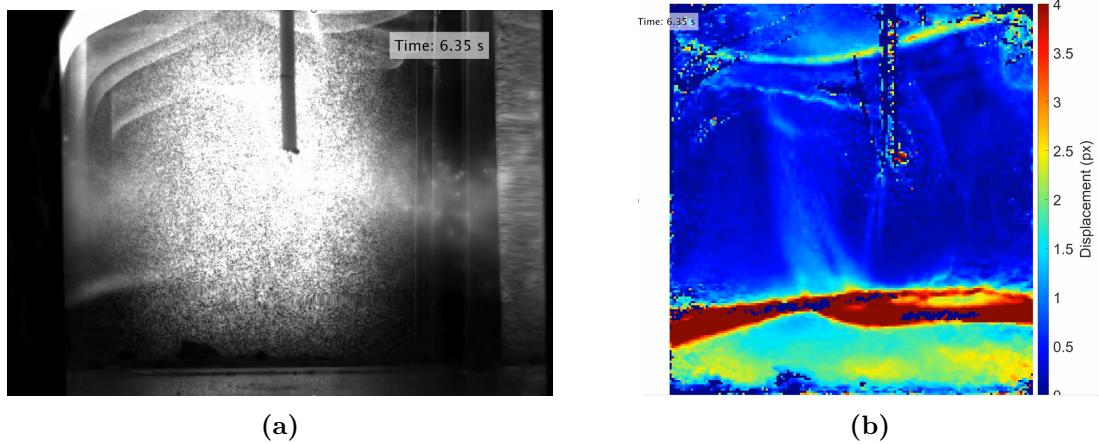


Figure 23: The displacement field grows in both size and intensity, reflecting elevated density gradients in the core as flame propagates

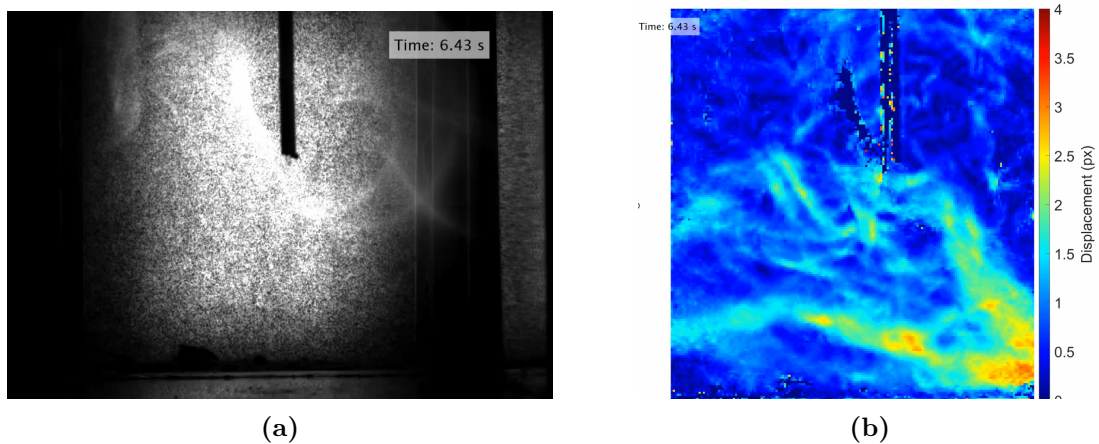


Figure 24: The BOS image (b) highlights the rapid density change as combustion products expand, confirming the transition from vapor mixing to flame-driven flow

4.2 Absorption and Temperature Plot

Complementing BOS, an absorption–temperature overlay plot was generated (see Figure 25), aligning absorption data with simultaneous temperature measurements. Unlike the relatively smooth concentration curves from other plots we have seen so far, the ignition overlay appeared more complex and irregular, reflecting:

- Rapid transition from dispersed vapor to high-temperature combustion products.
- Synchronization between the temperature peak and the combustion of the reactants.

This complexity supports the interpretation of a Mode I ignition, where rapid, energetic combustion creates sharp gradients in both fuel concentration and temperature.

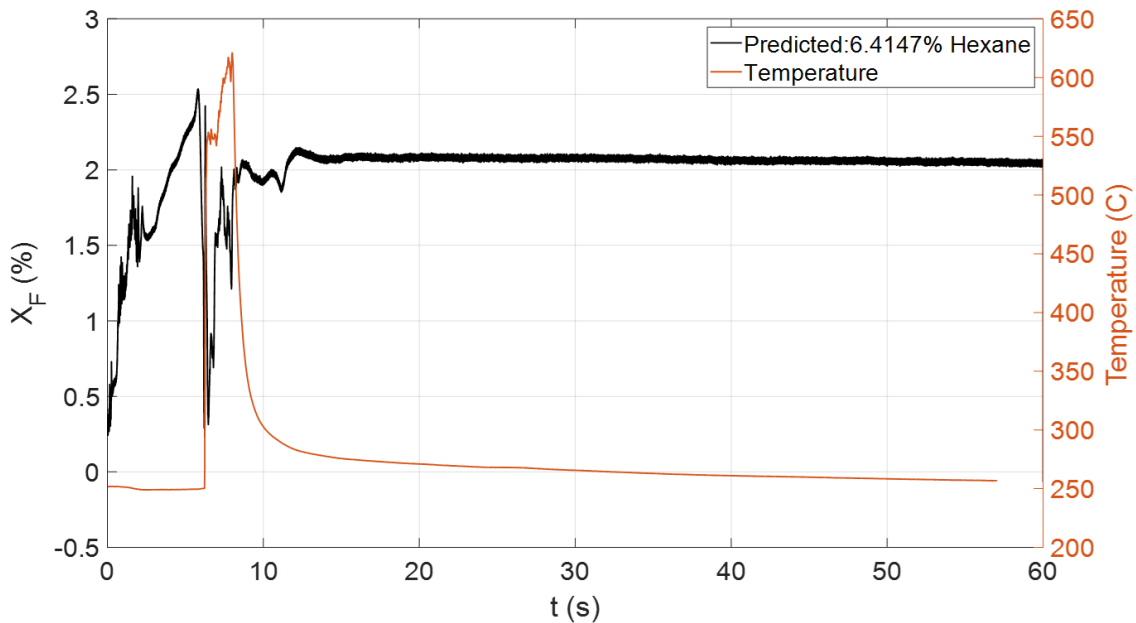


Figure 25: Ignition overlay plot showing irregular and complex absorption–temperature behavior. Unlike smoother concentration profiles from non-ignition tests, this curve reflects the rapid transition from dispersed vapor to combustion products, with strong fluctuations in absorption intensity. The complexity is consistent with a Mode I ignition event, characterized by energetic, uneven flame propagation and sharp coupled gradients in concentration and temperature.

4.3 New Cell Design Evaluation

Following the ignition test with hexane at $T(\text{cell}) = 250 \text{ } ^{\circ}\text{C}$, the performance of the redesigned cell was assessed in terms of usability, durability, and experimental reliability. The results revealed both strengths and weaknesses of the new setup:

Pros:

- Simplified injection and window operation increased convenience.
- Faster manipulation and turnaround - minimized heat losses.

Cons: While generally robust, the design showed one clear limitation: the ceramic component was ejected under high pressure caused by the ignition event, posing a durability concern.

5 Conclusions and Future Work

The ASTM-E659 setup successfully enabled controlled investigation of hexane vaporization and ignition dynamics. Over the course of thirty non-reactive tests, the repeatability of the system was investigated, with vapor concentrations aligning closely with theoretical expectations. Repeatability was limited by mechanical issues such as interrupted injections and volume losses. Loss of even a single droplet during injection directly affects repeatability because the injected volume is on the order of microliters. This makes comparisons across tests more difficult, as deviations are no longer due to fuel behavior but to inconsistencies in injection. Convection experiments further revealed that thermal gradients strongly influence the mixing rate of vapor, even though the final vapor concentration is governed primarily by thermodynamic constraints. Maintaining a stable thermal environment inside the cell is crucial for obtaining accurate and repeatable results. For this reason, strict attention to thermal management — through insulation to minimize heat losses during injection — is essential for ensuring that observed ignition events truly reflect the intrinsic properties of the fuel rather than artifacts of the apparatus. These observations and analysis confirmed both the sensitivity of the setup to small procedural variations and the importance of refining injection procedures to ensure reproducibility. The ignition test with 200 μL of hexane at 250 °C produced a Mode I ignition event, marked by rapid flame propagation and strong thermal feedback. BOS visualization revealed localized gradients in vapor dispersion, while the absorption–temperature overlay plot highlighted the inherently complex coupling between vapor concentration and thermal dynamics during ignition. Together, these diagnostics confirm the value of multi-modal measurements for interpreting ignition behavior.

The redesigned test cell showed notable improvements:

- Simplified injection and window operation enhanced convenience.
- Faster manipulation minimized thermal losses, enabling quicker test turnaround.

One clear limitation was also identified: the ejection of a ceramic component during ignition, attributed to pressure buildup. While this did not compromise the main functionality, it highlights the need for material and structural reinforcement in high-pressure scenarios.

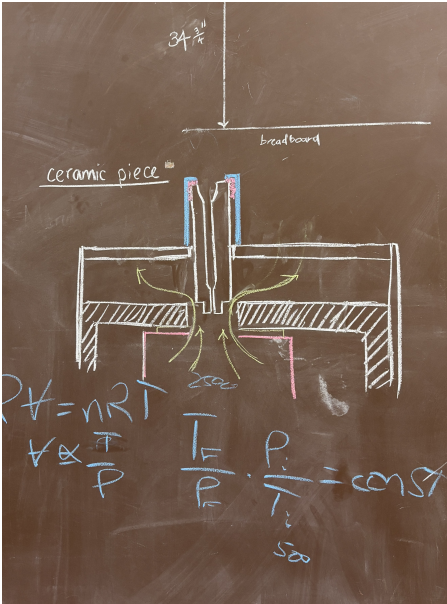
Future Work

Building on these findings, several directions for refinement and extension emerge:

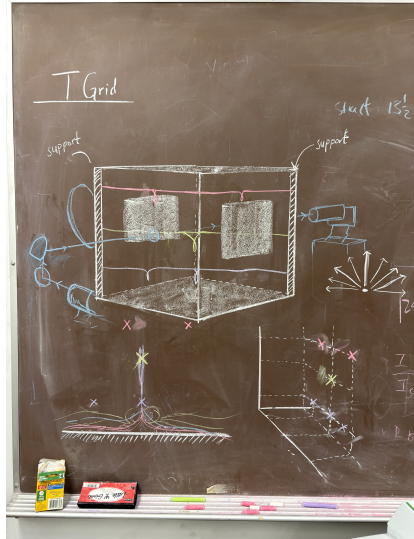
- Injection System Refinement – Further development of the needle guide and thermocouple placement is needed to improve on the accuracy of the instrument.
- Structural Improvements - Designing a pressure management system and support system for the ceramic piece to reduce risks of ejection under ignition pressures.
- Thermocouple Grid - To better capture the spatial variations in temperature that influence ignition behavior, a thermocouple grid
- More Testing – Repeating the methodology with different conditions would generalize the results and deepen the understanding of ignition mechanisms.

Some sketch ideas are presented in Figure 26.

In summary, the modified setup has demonstrated strong potential as a versatile platform for studying autoignition phenomena. With continued improvements in injection reliability, structural robustness, and diagnostic capability, the system can evolve into a powerful tool for probing fundamental questions of vaporization, convection, and ignition across a wide range of fuels and operating conditions.



(a) Ceramic Holder – Installed at the top of the cell to secure the ceramic guide and prevent it from being ejected during operation. The design includes a small clearance above the guide, lined with a soft material, to absorb impact energy and protect the ceramic from fractures.



(b) Thermocouple Grid – Designed with thermocouples arranged diagonally across the cell, but offset from the centerline to allow unobstructed passage of the injection needle. This layout enables temperature mapping of the vapor field at multiple locations, capturing spatial variations in thermal activity without interfering with fuel delivery.

Figure 26: Sketch ideas for future designs

Acknowledgements

This work was carried out in the Explosion Dynamics Laboratory of the California Institute of Technology and was partially supported by The Boeing Company during the summer of 2025. I gratefully acknowledge Professor Joseph Shepherd and Dr. Charline Fouchier for their invaluable mentorship and guidance throughout this project. Their expertise and critical feedback were essential in the design of the experiments and the interpretation of the results. I also extend my gratitude to Mr. Mack and Mrs. Haq for their generous financial support as M.A.Q Lutful Haq SURF Fellow donors, without which this SURF project would not have been possible.

References

- [1] C Martin and J Shepherd. Autoignition testing of hydrocarbon fuels using the astm-e659 method. Technical report, Technical Report EDL2020. 001. Graduate Aeronautical Laboratories . . . , 2020.
- [2] Nicholas P Setchkin. Self-ignition temperatures of combustible liquids. *Journal of Research of the National Bureau of Standards*, 53(1):49, 1954.
- [3] Michael G Zabetakis, Aldo L Furno, and George W Jones. Minimum spontaneous ignition temperatures of combustibles in air. *Industrial & Engineering Chemistry*, 46(10):2173–2178, 1954.
- [4] Branson Davis, Charline Fouchier, and Joseph E Shepherd. Fluid motion and heat transfer in an astm-e659 apparatus. *Journal of Loss Prevention in the Process Industries*, 94:105558, 2025.
- [5] H. Ramsperger. *Ignition of aviation fuels and surrogates in hot air atmospheres – Parametric analysis on the ASTM injection system*. EDL Publications, California Institute of Technology, 2024.
- [6] Charline Fouchier and Joseph Shepherd. Astm-e659 standardized test analysis and results for synthetic paraffinic kerosene. *Journal of Loss Prevention in the Process Industries*, 94:105568, 2025.
- [7] ASTM International. Standard test method for autoignition temperature of liquid chemicals. ASTM-E659, 2005.

Appendix

A. Temperature Tables

Test	Fuel Quantity (μL)	T_bottom (set)	T_top (set)	T(cell)	Injection speed	ΔT
Test_001	100	100 (104.6)	100 (101.7)	99	5 mL/min	0
Test_002	100	100 (104.6)	100 (101.7)	99	5 mL/min	0
Test_003	100	99 (104.6)	99 (101.7)	98	5 mL/min	0
Test_004	100	99 (104.6)	99 (101.7)	98	5 mL/min	0
Test_005	100	99 (104.6)	99 (101.7)	99	5 mL/min	0
Test_006	100	99 (104.6)	99 (101.7)	99	5 mL/min	0
Test_007	100	103 (109.6)	99(101.7)	100	5 mL/min	4
Test_008	100	104 (109.6)	100(101.7)	100	5 mL/min	4
Test_009	100	104 (109.6)	99(101.7)	100	5 mL/min	5
Test_010	100	99 (104.6)	99 (101.7)	98	5 mL/min	0
Test_011	100	99 (104.6)	99 (101.7)	97	5 mL/min	0
Test_012	100	100 (104.6)	99 (101.7)	99	5 mL/min	0
Test_013	100	99 (104.6)	99 (101.7)	99	5 mL/min	0
Test_014	100	100 (104.6)	100 (101.7)	99	5 mL/min	0
Test_015	100	100 (104.6)	100 (101.7)	99	5 mL/min	0
Test_016	100	108(115.0)	100(101.7)	101	5 mL/min	8
Test_017	100	108(116.0)	100(101.7)	103	5 mL/min	8
Test_018	100	109(116.0)	100(101.7)	101	5 mL/min	9
Test_019	100	130(142.0)	106(100.0)	115	5 mL/min	24
Test_020	100	133(142.0)	106(100.0)	118	5 mL/min	27
Test_021	100	133(142.0)	119(100.0)	125	5 mL/min	14
Test_022	100	134(142.0)	119(100.0)	124	5 mL/min	15
Test_023	100	134(142.0)	119(100.0)	124	5 mL/min	15
Test_024	100	134(142.0)	119(100.0)	124	5 mL/min	15
Test_025	100	163(175.0)	142(100.0)	150	5 mL/min	22
Test_026	100	173(185.0)	152(100.0)	160	5 mL/min	21
Test_027	100	173(185.0)	151(100.0)	160	5 mL/min	22
Test_028	100	185(200.0)	160(100)	170	5 mL/min	25
Test_029	100	187(200.0)	167(100.0)	175	5 mL/min	20
Test_030	100	186(200.0)	166(100.0)	174	5 mL/min	20

Figure 27: Temperature conditions for all tests carried

B. CAD Drawings

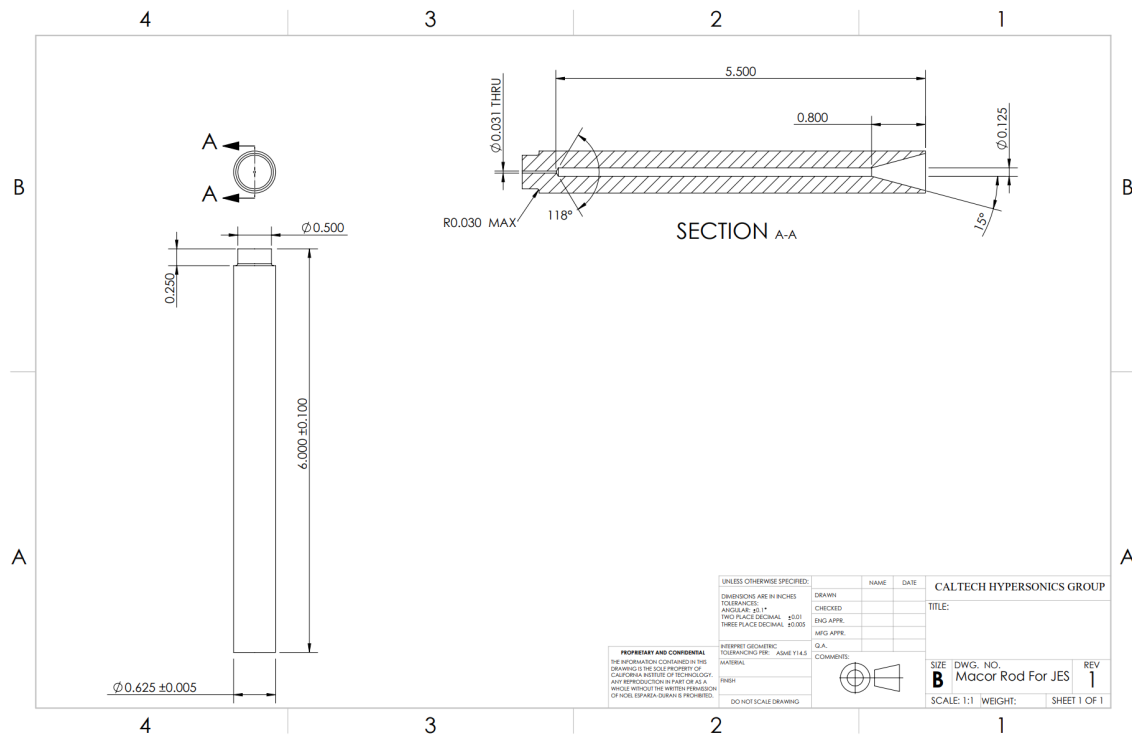


Figure 28: Ceramic Guide

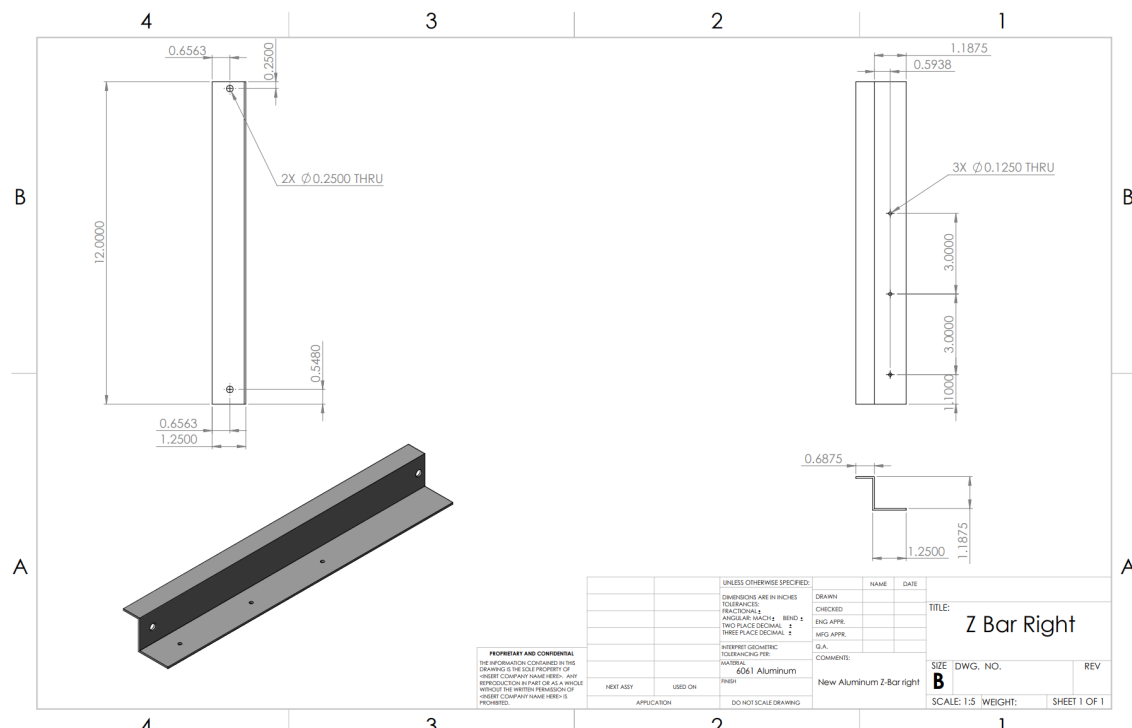


Figure 29: Z-Bar (Guiding Channel)

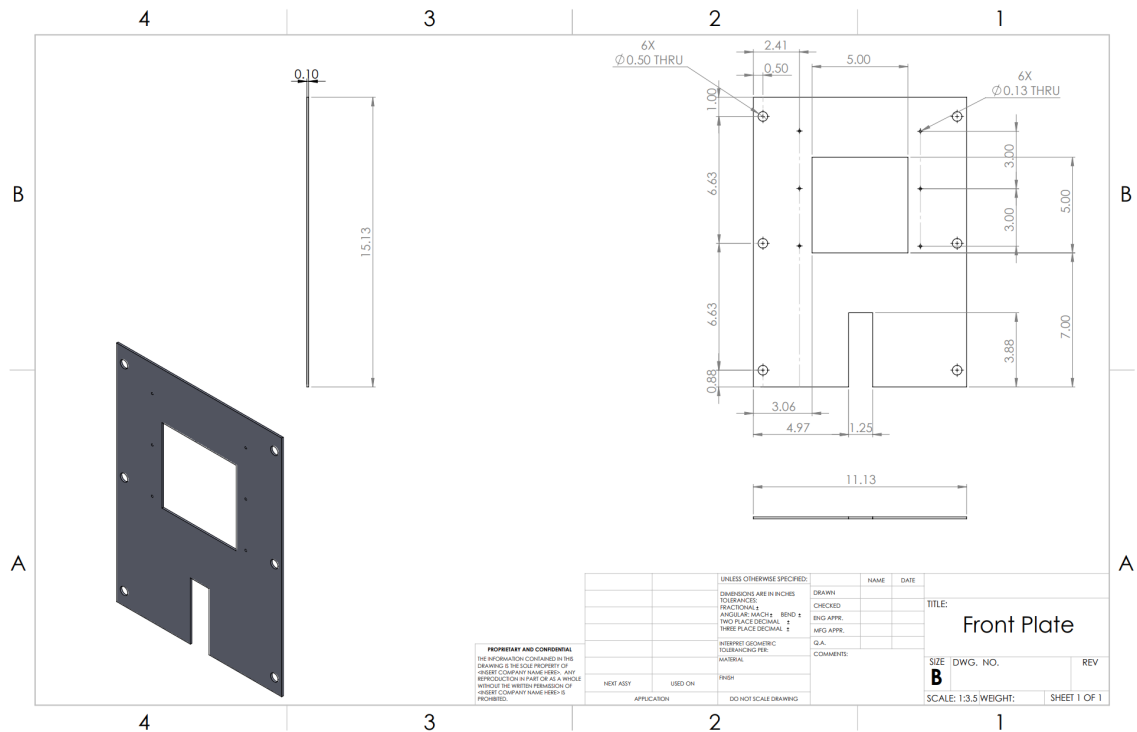


Figure 30: Front Plate

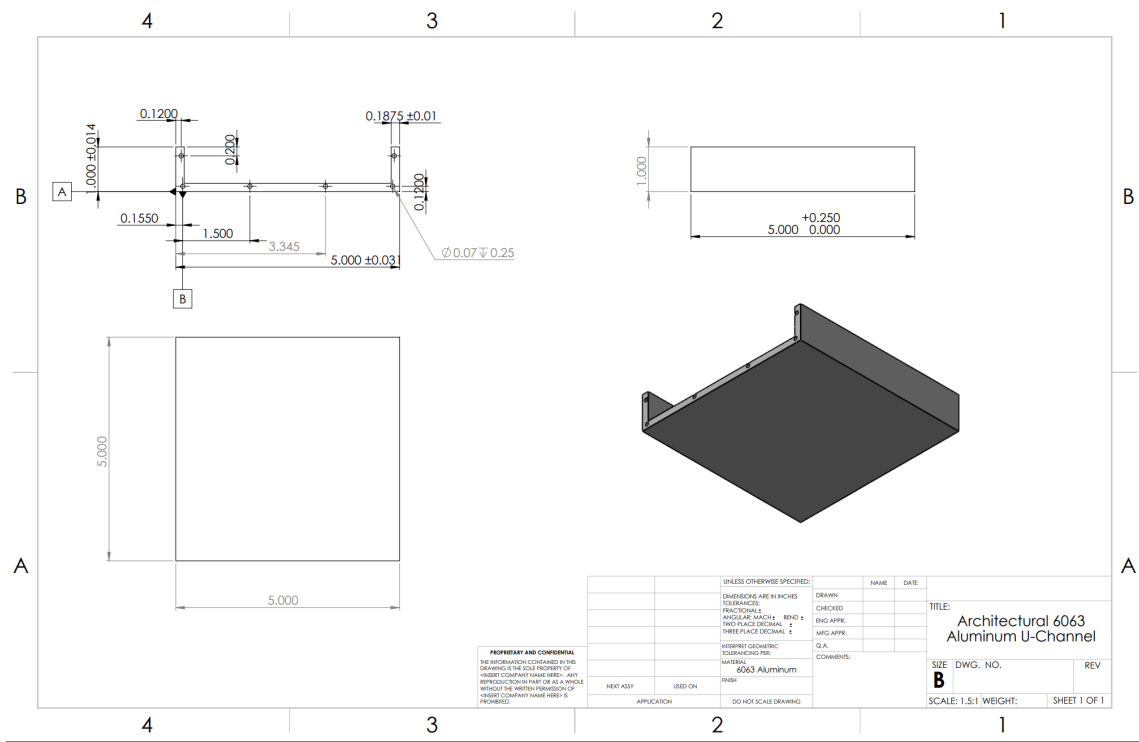


Figure 31: U-Channel(Shutter Body)

C. Bill of Materials

	PART #	DESCRIPTION	QTY	INDIVIDUAL COST	SUBTOTAL	LINK	Notes
MC MASTER CARR ORDER	3071T1	Mounted Pulley for Rope-for Horizontal Pull	4	8.88	35.52	https://www.mcmaster.com/3071T1/	
	47065T103	T-Slotted Framing 2ft	5	26.37	131.85	https://www.mcmaster.com/47065T103	
	47065T103	T-Slotted Framing 1ft	2	14.92	29.84	https://www.mcmaster.com/47065T103	
	8499K519	Easy-to-Machine Glass-Mica Ceramic Low-Stretch Rope - for Lifting	1	67.14	67.14	https://www.mcmaster.com/8499K519/	
	222T11	Silver Gusset Bracket, 3"(1.5in)	1	7.5	7.5	https://www.mcmaster.com/222T11	5/8" Diameter Rod, 6" Long
	47065T762	Silver 90 Degree Angle Bracket (1.5in)	8	15.2	121.6	https://www.mcmaster.com/47065T762/	Easy-Splice, 1/8" Diameter, 10 ft
	47065T578	Silver Tee Surface Bracket(1.5 in)	2	25.77	51.54	https://www.mcmaster.com/47065T578/	
	484AN93	Silver Corner Bracket	2	29.5	59	https://www.mcmaster.com/484AN93/	
	47065T831	Adhesive-Back Chemical-Resistant Slippery PTFE Film	8	9.71	77.68	https://www.mcmaster.com/47065T831/	
	220B791	Architectural 6063 Aluminum U-Channel Rigid Mineral Wool Insulation Sheet	1	124.56	124.56	https://www.mcmaster.com/220B791/	12" Wide, 0.06" Thick
	9001K906	Multipurpose 6061 Aluminum Z-Bar	1	87.82	87.82	https://www.mcmaster.com/9001K906/	
	9328K512	Alloy Steel Low-Profile Socket Head Screw	4	43.66	174.64	https://www.mcmaster.com/9328K512/	
	7062T32	6061 Aluminum Sheet	4	8.56	34.24	https://www.mcmaster.com/7062T32/	1.25"
	92220A311	Black-Oxide Alloy Steel Flanged Button Head Screw	2	20.41	40.82	https://www.mcmaster.com/92220A311/	
	89015K128	Silver Flush Tee Bracket for 1.5"	1	3.5	3.5	https://www.mcmaster.com/89015K128/	
	89015K964	Black-Oxide Alloy Steel Flanged Button Head Screw	2	90.98	181.96	https://www.mcmaster.com/89015K964/	Aluminum cell wall (0.1"), 12" x 48"
	3136N161	Tight-Tolerance Low-Carbon Steel Bar	1	20.71	41.42	https://www.mcmaster.com/3136N161/	
	9135A5177	Black-Oxide Alloy Steel Flanged Button Head Screw	1	10.94	10.94	https://www.mcmaster.com/9135A5177/	1/4"-20 Thread, 5/16" Long (pack of 10)
	9517K374	Tight-Tolerance Low-Carbon Steel Bar	1	17.56	17.56	https://www.mcmaster.com/9517K374/	
					1067.17		

Figure 32: Finalized Bill of Materials